

# Flatband slows down polariton dynamics in strongly coupled cavities

Yesenia A García Jomasa,<sup>1</sup> Brenda Vargas,<sup>1</sup> David Ley Domínguez,<sup>1</sup> Román J. Armenta-Rico,<sup>1</sup> Huziel E. Saucedo,<sup>1</sup> César L Ordoñez-Romero,<sup>1</sup> Hugo A Lara-García,<sup>1</sup> Arturo Camacho-Guardian,<sup>1</sup> and Giuseppe Pirruccio<sup>1</sup>

<sup>1</sup>*Instituto de Física, Universidad Nacional Autónoma de México, Apartado Postal 20-364, Ciudad de México C.P. 01000, Mexico*

(Dated: September 12, 2023)

Flatbands in condensed-matter, atomic physics, and quantum optics stand as the basis for several strongly correlated quantum many-body phenomena such as Wigner crystallization, the fractional quantum Hall effect and Moiré-related physics. Besides inspiring analogies among diverse physical fields, flatbands are highly sought-after in photonics because they allow unconventional light flows such as slow-light. Here, we realize room-temperature slow-light with Frenkel polaritons excited across two strongly coupled cavities. We demonstrate the formation of a tuneable flatband appearing in absence of a periodic in-plane potential. Our simple photonic architecture enables the unique spatial segregation of photons and excitons in different cavities and maintains a balanced degree of mixing between them. This unveils a dynamical competition between many-body scattering processes and the underlying polariton nature which leads to an increased fluorescence lifetime. The polariton features are further revealed under appropriate resonant pumping, where we observe suppression of the flatband polariton fluorescence intensity.

In condensed matter physics, flatbands have led to the achievement of several breakthroughs, including strongly correlated electronic states [1], non-conventional superconductivity [2–4], and topological phases of matter in two-dimensional materials [5]. Similarly, within photonic systems, the presence of flat optical bands is highly desirable, as they could prompt the generation of strongly correlated photonic states [6–10]. This is not only fundamentally relevant, but could also have an impact on energy harvesting, sensing, and information processing. Slow-light, the phenomenon of controlling and manipulating dispersion of light [11], has received attention in quantum optics [12], atomic physics [13, 14] and condensed matter [15, 16]. The ability to tune the dispersion of light yields new opportunities to design light-matter interactions and non-linear optical devices [17, 18]. In the quantum domain, slow-light is typically understood in terms of polaritons [19], hybrid light-matter quasiparticles that arise from mixing a photon with an elementary matter excitation. The propagation of light in the form of a dark-state polariton within a medium can be slowed down and even stopped by heavily unbalancing the mixture of light and matter. In atomic gases, slow-light is typically accompanied by the phenomenon of electromagnetically induced transparency whereby, assisted by a control laser field, light propagates undamped in a typically opaque medium [20, 21].

## Slow-light and intercavity organic polaritons

Polaritons found in both organic and inorganic semiconductors have demonstrated a high degree of flexibility to control the internal energy structure and dynamics, unfolding alternative routes, [22–28] including the use of photonic lattices to craft flatbands [29–32].

In this article, our proposal involves the successful implementation of a polariton flatband at room temperature through the strong coupling of a photonic cavity with a polaritonic cavity. The dispersion of the so-formed intercavity polaritons is tailored by tweaking the three-

energy-level diagram. This adjustment of the diagram allows us to fine-tune the dispersion of the resulting intercavity polaritons. The observed flatband signals the transition from a bright to dark polariton state characterized by a stretched polariton lifetime. The dark nature of such intercavity flat polariton is indirectly confirmed by its suppressed light-emission obtained under careful resonant pumping.

Our findings suggest that reducing polariton group velocity is akin to generating slow-light in atomic gases when the condition for electromagnetically induced transparency is fulfilled. Furthermore, inter-cavity polaritons open up the quantum tomography protocols for local and independent measurements of the photonic and molecular degrees of freedom.

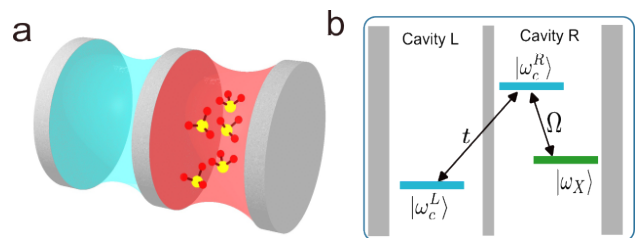


FIG. 1. **Experimental setup.** (a) Representation of the hybrid photonic-polaritonic coupled system. (b) Relevant energy levels:  $|\omega_c^{(L)}\rangle$ ,  $|\omega_c^{(R)}\rangle$  and  $|\omega_X\rangle$  represent the left photon, right photon and exciton state, respectively. Photons tunnel from left to right cavity with a hopping amplitude  $t$ .  $\Omega$  is the light-matter coupling.

Up until now, the exploration of strongly coupled photonic cavities has primarily centered around photonic crystal cavities [33], micro-rings [34], and whispering-gallery modes [35]. In the context of semiconductor microcavities, double-well potentials have led to the realization of phenomena like Josephson oscillations and self-trapping with intercavity polaritons, [36, 37] and

have been recently proposed for quantum chemistry control [38].

To realize slow-light we designed a three-level energy scheme representing two strongly coupled cavities. This set-up reminds of the  $\Lambda$ -scheme commonly employed in quantum control experiments. Our system, sketched in Fig. 1(a), is composed by two cavities, labelled (Left) and (Right), coupled *via* a thin mirror. The left cavity, represented by  $|\omega_c^{(L)}\rangle$ , is purely photonic, whereas the right cavity host both photons and excitons, identified by  $|\omega_c^{(R)}\rangle$  and  $|\omega_c^{(X)}\rangle$ , respectively. The Hamiltonian of the system is given by

$$\hat{H} = \sum_{i=L,R} \omega_c^i(\theta) \hat{a}_i^\dagger \hat{a}_i - t(\hat{a}_L^\dagger \hat{a}_R + \hat{a}_R^\dagger \hat{a}_L) + \omega_X \hat{x}^\dagger \hat{x} + \Omega (\hat{x}^\dagger \hat{a}_R + \hat{a}_R^\dagger \hat{x}) \quad (1)$$

where  $\omega_c^{(L/R)}(\theta)$  indicates the energy of the left/right cavity photons, which are created with the operator  $\hat{a}_{L/R}^\dagger$ . Here, the angle  $\theta$  corresponds to the incident angle of light injected to the right cavity. In Fig. 1(b), the photon hopping is characterised by a tunneling amplitude  $t$ , while the light-matter coupling is given by the Rabi frequency  $\Omega$ .

The sample consists of two vertically stacked nanocavities fabricated on a glass substrate by a sequence of multiple sputtering and spin-coating steps. The front, middle and back mirrors are made by Ag and their thickness equal to 20 nm, 20 nm and 300 nm, respectively. The middle mirror width determines the tunneling amplitude  $t$ . The Left nanocavity is filled with polymethyl methacrylate (PMMA), whereas the Right one embeds a dye-doped polyvinyl alcohol (PVA) layer. The excitonic content is provided by a high concentration of homogeneously dispersed Erithrosine B (ErB) molecules [39]. The absorption spectrum of the active medium exhibits a main peak around  $\omega_X \approx 2.24\text{eV}$  associated to a principal exciton resonance and a second peak at  $\omega_v \approx 2.4\text{eV}$  related to the first vibron mode.

The polymer thickness of the Left cavity features a slow wedge which provides us the possibility of fine tuning  $|\omega_c^{(L)}\rangle$  in a wide photon energy range. When the resonance frequency of the left cavity at normal incidence matches the exciton one, an intercavity polariton,  $|D(\theta = 0)\rangle$ , emerges

$$|D(\theta = 0)\rangle = \frac{\Omega}{\sqrt{\Omega^2 + t^2}} |\omega_c^{(L)}(\theta = 0)\rangle - \frac{t}{\sqrt{\Omega^2 + t^2}} |\omega_X\rangle, \quad (2)$$

solely formed by the superposition of the left cavity photon and the exciton. Importantly, the right cavity photon

does not participate in the formation of this polariton state. Further details on the geometrical order of the cavities are provided in the Supplementary Information.

In Fig. 2(a)-(c), we show the local band structure of the coupled cavity system measured via Fourier microscopy, which demonstrates that the  $\Lambda$ -scheme yields a middle polariton (MP) state with energies close to the bare exciton one. Fine-tuning of the MP energy is accomplished by leveraging the wedged PMMA thickness. The MP state shows a reduced dispersive character compared to the upper (UP) and lower polariton (LP) and flattens for a specific value of the thickness of the photonic cavity.

To theoretically understand our results, we introduce the detuning,  $\delta = \omega_c^{(L)} - \omega_X$ , and the imaginary-time Green's function of the system,  $\mathcal{G}_{\alpha,\beta}(\tau) = -\langle T_\tau [\hat{\psi}_\alpha(\tau) \hat{\psi}_\beta^\dagger(0)] \rangle$ , where the subindices  $\alpha, \beta$  correspond to the left/right cavity photon and exciton, respectively. The fields  $\psi$  and  $\psi^\dagger$  evolve according to Eq. 1. We define the spectral function of the left cavity photon as  $A(\omega) = -2\text{Im}\mathcal{G}_{11}(\omega)$  and we plot it in Fig. 2(d)-(f) for three values of  $\delta$ , showing a very good agreement with the experimentally observed reflectance. By continuously varying the left cavity thickness, its photon energy is driven in resonance with the exciton energy. Furthermore, the energy of the polariton states obtained from our theory and plotted with dashed curves on the reflectance maps, Fig. 2(a)-(c), provide an excellent quantitative understanding of the system.

We obtain a reduction of the photonic dispersion of the left cavity photons

$$\omega_{\text{MP}}(\theta) \approx \omega_X + [\omega_c^L(\theta) - \omega_X] \frac{1}{1 + (\frac{t}{\Omega})^2}, \quad (3)$$

this means that the dispersion of the MP is controlled by the tunnelling ratio,  $t$ , which can be tailored by means of the middle mirror thickness. On resonance, the MP emerges at the energy of the bare exciton, its dispersion reduced by a factor 4-8 compared to the energies of the upper and lower polaritons, this leads to a pronounced flatband over a wide range of incident angles. While the dispersion can be further reduced, this would be at the expense of strongly suppressing the photonic component.

The character of the MP is clearly unveiled once it is written in terms of the bare photon and exciton states  $|\text{MP}\rangle = \sum_\alpha \mathcal{C}_{\text{MP}}^\alpha |\alpha\rangle$ . The amplitude of its Hopfield coefficients  $Z_{\text{MP}}^\alpha = |\mathcal{C}_{\text{MP}}^\alpha|^2$  in Fig. 2(g)-(i) demonstrates that the MP decouples from the right cavity photons for  $\delta = 0$ . Furthermore, Fig. 2(i) shows that the Hopfield coefficients remain invariant along the angular region where the MP is flat. There, the MP has only non-vanishing Hopfield coefficients of the left cavity photon and the exciton. For conventional polaritons arising in two-level schemes, suppression of the polariton dispersion can only be achieved by compromising the degree of mixing between photons and excitons. This means that only far-detuned polaritons asymptotically exhibit quasi-flat dispersion and, thus, are formed by a large exciton component and negligible photon contribution. In contrast,

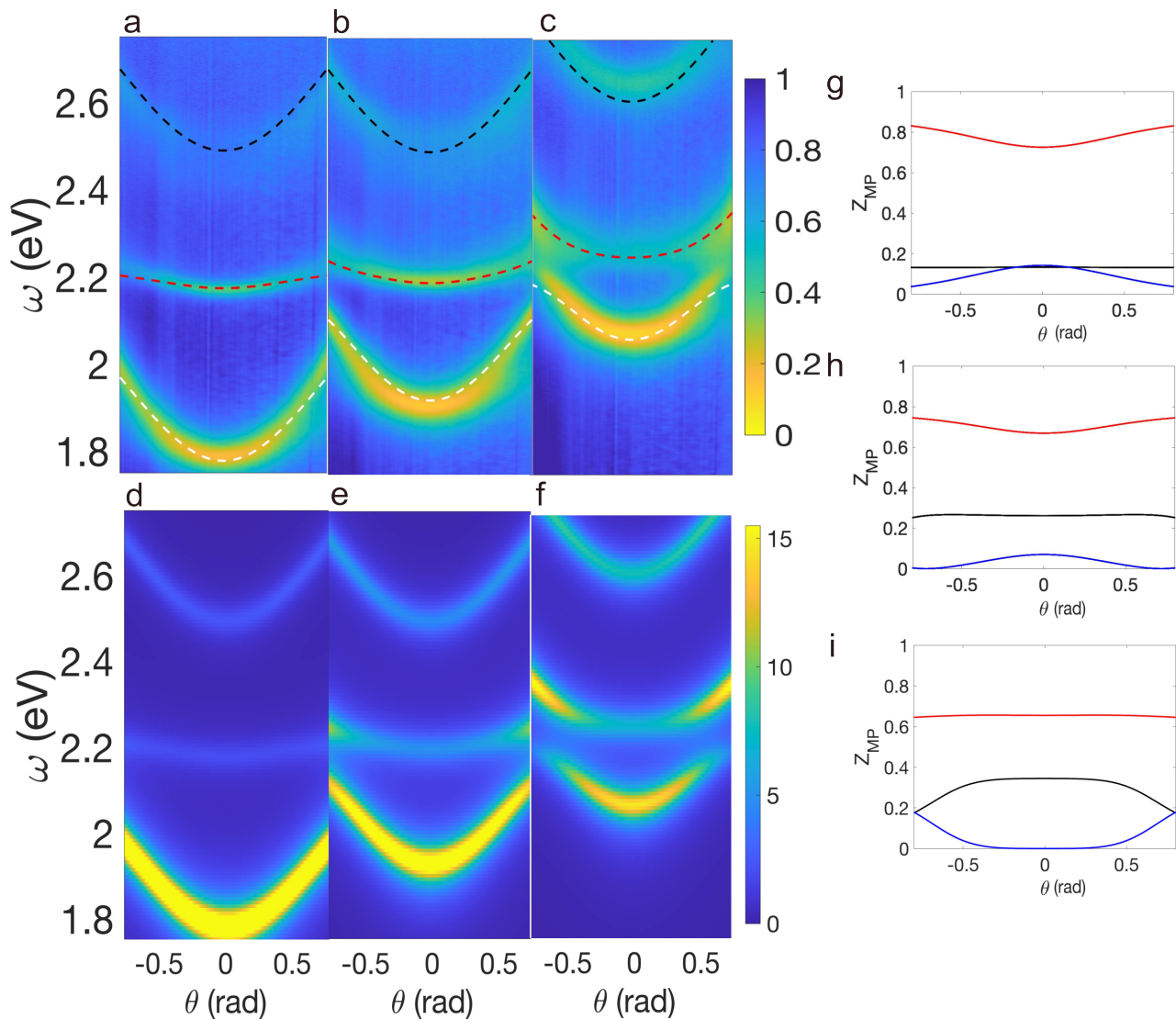


FIG. 2. **Intercavity polaritons.** (a)-(c) s-polarized reflectance as a function of the angle of incidence and photon energy for (a)  $\delta/\text{eV} = -0.37$ , (b)  $\delta/\text{eV} = -0.18$  and (c)  $\delta/\text{eV} = 0$ . The white, red, and black dashed curves correspond to the theoretical fitting of the energies of the lower, middle, and upper polariton respectively. (d)-(f) Spectral function,  $A(\mathbf{k}, \omega)$ , calculated for the same detunings as in (a)-(c). Middle polariton Hopfield coefficients for (g)  $\delta/\text{eV} = -0.37$ , (h)  $\delta/\text{eV} = -0.18$  and (i)  $\delta/\text{eV} = 0$ . The black, blue and red curves correspond to the left cavity photon, right cavity photon and exciton component, respectively.

our three-level design allows for flatband polaritons and slow-light retaining a significant photonic component of circa 40%.

#### Short-time dynamics.

Now we focus on the effect of the vanishing curvature of the MP, hinting at a mechanism analogous to the charge population trapping observed in atomic electromagnetically induced transparency. For this, we measure the prompt fluorescence decay employing the time-correlated single-photon counting technique. We explore the dynamics of the LP and MP and relate them with the corresponding photon component. The coupled cavities are pumped off-resonantly with laser pulses centered around 2.42 eV.

Figure 3(a) displays decays for two detunings used in Fig. 2, i.e.,  $\delta/\text{eV} = 0$  and  $\delta/\text{eV} = -0.37$ . In the considered time interval, all decays are well described by two time constants. For our analysis we focus initial dynamics illustrated in the pink shaded region. We model the evolution assuming a dynamical equation of the form  $C(t) = A \exp(-\Gamma t) + (1 - A) \exp(-\eta t)$ , normalized to  $C(t = 0) = 1$ . Figure 3(a) shows that this model (solid curves) provides a very good fit to the experimental data (points). We obtain that the LP dynamics is dominated by a single exponential with  $\Gamma_{\text{LP}}(\delta = 0) = 3.25 \text{ ns}^{-1}$  and  $A_{\text{LP}} = 0.94$ , while  $\Gamma_{\text{LP}}(\delta = -0.37) = 3.0 \text{ ns}^{-1}$  with  $A = 0.86$ . On the other hand, we find a richer dynamics for the MP, whose dynamics is characterised by

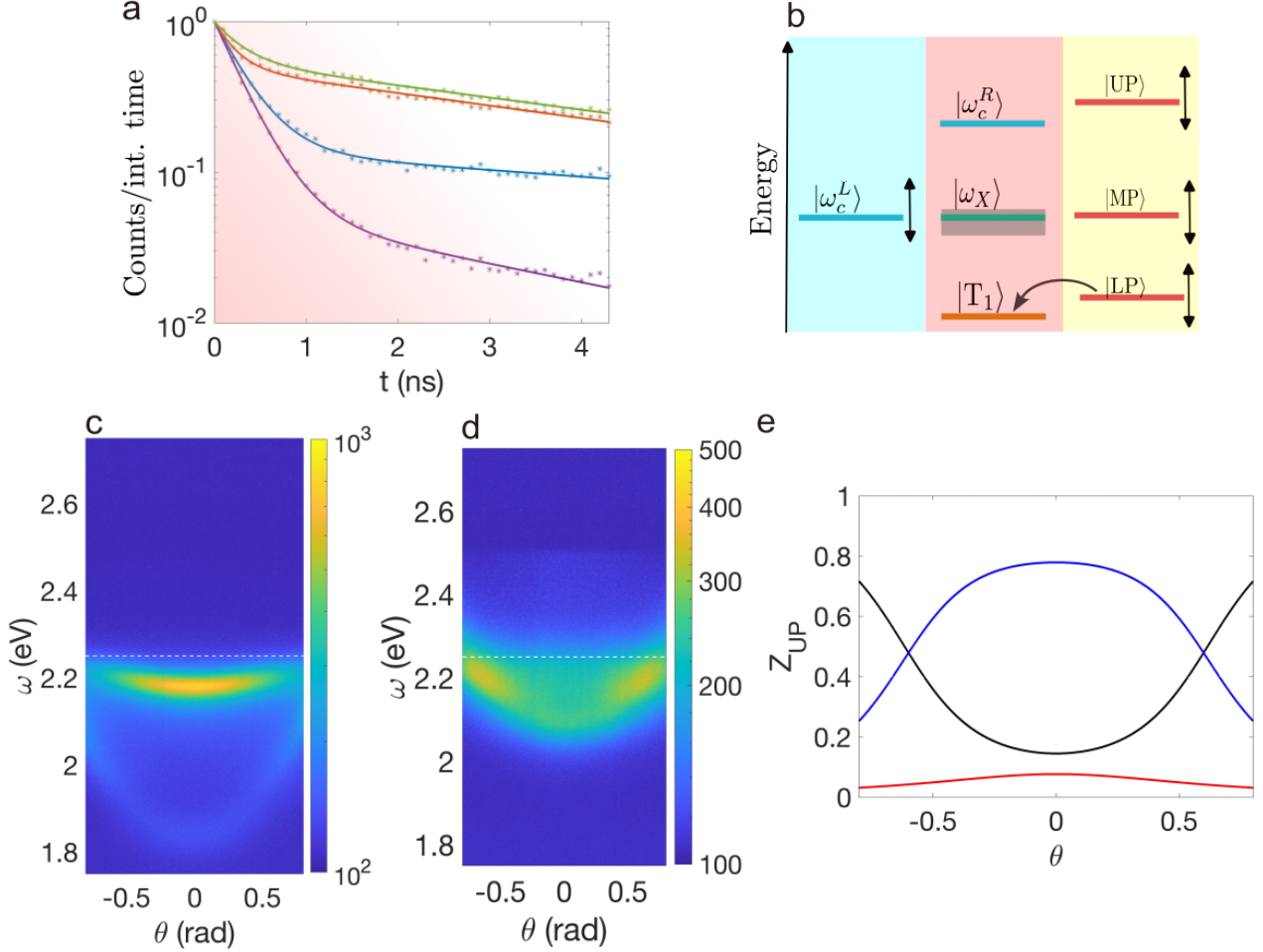


FIG. 3. **Short-time dynamics and dark-state polaritons.** (a) Normalized fluorescence lifetime showing the short-time dynamics of the middle and lower polaritons. The dynamics of the MP is displayed with orange and green asterisks for  $\delta/eV = -0.37$  and  $\delta/eV = 0$ , respectively. The LP decay is illustrated with blue and purple asterisks for  $\delta/eV = -0.27$  and  $\delta/eV = 0$ , respectively. Shaded pink depicts the region where the fastest decay component dominates the early polariton dynamics. (b) Sketch of the relevant energy levels. Fine-tuning the left cavity photon energy, shifts the energy of the three polariton states. The grey area symbols the presence of the dark exciton reservoir. The triplet state of the ErB molecules,  $|T_1\rangle$ , influences the LP dynamics via intersystem crossing. (c)-(d) s-polarized fluorescence, expressed in counts per integration time, for  $\delta/eV = -0.37$  and  $\delta/eV = 0$ , respectively. The energy of the bare exciton is represented by the dashed white line. Photons are injected at  $\omega_p/eV = 2.6$  which lies at the energy of the upper polariton. (e) Hopfield coefficients of the UP for  $\delta/eV = 0$  showing that it is predominantly formed by right cavity photons. The black, blue and red curves correspond to the left cavity photon, right cavity photon and exciton component, respectively.

$\Gamma_{MP}(\delta = 0) = 0.18 \text{ ns}^{-1}$  and  $\eta_{MP}(\delta = 0) = 3.25 \text{ ns}^{-1}$  for the flatband condition, and  $\Gamma_{MP}(\delta = -0.37) = 0.19 \text{ ns}^{-1}$  and  $\eta_{MP}(\delta = -0.37) = 4.57 \text{ ns}^{-1}$  for the detuned case. In contrast to the LP, the weight of the exponentials for the MP is almost equally distributed as  $A(\delta = 0) = 0.55$  and  $A(\delta = -0.37) = 0.5$ . The significantly slower dynamics of the MP shown in Fig. 3(a) is consequence of the interplay between the two dynamical factors. Indeed, we observe that at very small times, in the linear regime  $C_{LP}(t) \approx 1 - \Gamma_{LP}t$ , whereas  $C_{MP}(t) \approx 1 - [A\Gamma_{MP} + (1 - A)\eta_{MP}]t = 1 - \gamma_{\text{eff}}t$ . On resonance,  $\delta = 0$ , we obtain  $\gamma_{\text{eff}} \approx 1.7 \text{ ns}^{-1}$  which is significantly smaller than the dominant decay rate of the

LP. We attribute this effect to a competition between a reduced photon component of the MP, which suppresses the damping rate, and the presence of the dark-states reservoir of exciton laying close to the energy of the MP, which may favour non-radiative scattering and accelerated decay. We observe that the dynamics of the MP is slower than LP one, even though the MP energetically lies on top of the reservoir of dark-state excitons (see Fig. 3(b)). Therefore, we conclude that the vanishing curvature of the MP and its concomitant dark nature produces a significant effect in the polariton dynamics in the nanosecond range.

Finally, we see that the decay of the LP becomes slower

as it approaches the energy of the ErB triplet state,  $|T_1\rangle$ . This is evident from the asymptotic intensity value of the decay curve which does not converge to the noise floor of the other curves. Here, intersystem crossing not only increases significantly the slow component of the decay, but also stretches the fast one, outcompeting the role played by the photonic Hopfield coefficients and producing long-lived polaritons.

### Photoluminescence

To further investigate the nature of the polariton states we now turn our attention to the steady-state fluorescence. The system is pumped with a CW laser emitting at  $\omega_p = 2.62\text{eV}$ , which corresponds to an off-resonant excitation for all negative detunings. This means that we inject photons approximately equally in both cavities and produce excitons in the right cavity. For  $\delta/\text{eV} = -0.37$ , the MP is formed almost equally by both left and right cavity photons, while LP is formed predominantly by left cavity photons. Thus, we observe a higher fluorescence intensity from the MP than from the LP, as seen in Fig. 3(c). In the Supplemental Information we show that as we decrease the detuning, the LP acquires a larger fraction of the photon and exciton component of the right cavity, which consistently conduces to an increased LP fluorescence.

However, as we approach the condition for  $\delta/\text{eV} = 0$ , the UP energy shifts until it matches the pump energy at normal incidence. As shown in Fig. 3(e), the UP for  $\delta/\text{eV} = 0$ , is primarily formed by right cavity photons. Therefore, this configuration preferentially injects photons into the right cavity. As we move towards the condition for flatband polariton, the right cavity photon component of the MP decreases until vanishing exactly. Decoupling the MP from the right cavity photons results in an inefficient excitation of the MP and, thus, a strongly suppressed MP fluorescence intensity, as demonstrated in Fig. 3(d), confirming the transition of the MP to a dark state.

### Conclusions and Outlook

We have experimentally demonstrated the formation of inter-cavity polaritons composed by the admixture of photons and excitons sitting in physically separated optical cavities. The three energy level  $\Lambda$ -scheme underpinning the physics of this system implies, on resonance, the existence of a polariton flatband. We observed the flattening of the middle polariton branch which transits smoothly to a dark state upon tweaking the photon-exciton detuning. This mechanism effectively decouples the flatband polariton from free space leading to slower short-time dynamics. On resonance, the absence of one of the photon states in the composition of the dark polariton is confirmed by the steady-state fluorescence, whose intensity is suppressed under resonant pumping of the upper polariton branch. The interplay of the polaritons with the exciton reservoir needs to be taken into account as this introduces entropically favored scattering paths that may hamper the observation of more exotic physics. However, we stress that the short-dynamics modification

hints at that slow-light possibly overcomes the effect of the reservoir. This motivates further studies on the interplay between the dark-state dynamics and the possible breakdown of quasiparticle picture [39–41].

Hybrid photonic-polariton systems are an ideal platform to explore many-body physics in multi-level coupled cavity systems.

This shares analogy to interlayer excitons observed in stacked 2D materials, where the indirect character of the interlayer excitons gives rise to strongly interacting many-body states [42], long-lived exciton-polaritons [43, 44], and new classes of polaritons [45, 46]. Inspired by how twistrionics in stacked 2D materials gave rise and non-conventional superconductivity [47], we envisage that polariton flatbands can be useful to increase polariton correlations and facilitate the observation of non-trivial quantum phases in lattices-free systems. Moreover, our strategy to generate slow-light does not compromise the photonic component of the flatband polariton, making it appealing for strongly correlated truly polariton states. The reduced in-plane propagation helps confining spatially polaritons without the additional complication of fabricating physical boundaries. This may lower the threshold needed for quantum phases transitions while maintaining the architecture of the system simple. Furthermore, the quantum entanglement between the photonic and molecular degrees of freedom may be unraveled by exploiting the spatially indirect character of the intercavity polariton.

### Methods

#### *Sample fabrication*

The sample is composed by two vertically stacked Fabry-Pérot cavities fabricated on a glass substrate  $10 \times 10 \text{ mm}^2$  by multiple successive sputtering and spin-coating steps. The bottom 300 nm-thick Ag mirror was fabricated by magnetron sputtering operated at room temperature and a base pressure of approximately  $10^{-6}$  Torr which, during deposition, is pressurized with argon flow to  $3 \times 10^{-3}$  Torr. We deposited 99.99% purity Ag at a rate of 0.08 nm/s. The active layer of the first cavity is obtained starting from a solution of 25 mg of polyvinyl alcohol (PVA, Mowiol 44-88, 86.7-88.7% hydrolyzed, Mw  $\approx 205\,000$  g/mol) dispersed in 1 mL of distilled water. Then, 9.8 mg of Erythrosin B (ErB, Sigma Aldrich with dye content  $>90\%$ ) was added to the PVA/water solution, yielding a 0.5 M concentration. The ErB/PVA thin films were deposited by spin-coating at 2100 rpm using a  $0.45 \mu\text{m}$  pore PTFE syringe filter, obtaining approximately 120 nm thickness. The first cavity is completed by fabricating a 20 nm-thick middle mirror on top of the active layer. The second cavity is formed by a Poly-methyl methacrylate (PMMA, Mw  $\approx 120\,000$  g/mol) layer embedded between the middle and top mirror. This layer is obtained starting from a 25 mg/mL solution of PMMA. The solution is spin-coated at 2600 rpm for 60 s using a  $0.45 \mu\text{m}$  pore PTFE syringe filter and provides a slow thickness gradient centered around 140 nm. Using PMMA instead of PVA avoids the formation of micro-

bubbles at the surface of the second cavity.

#### *Experimental set-up*

Energy-momentum spectroscopy is performed in a homemade confocal Fourier optical microscope. Imaging the back-focal plane of a high numerical aperture microscope objective onto the entrance slit of a spectrograph (Kymera 328i, Andor) coupled to a sCMOS camera (Zyla 4.2P, Andor) is done by a Bertrand lens and provides direct access to the angular- and spectral-resolved reflectance. In our set-up the sample is illuminated through a Plan Fluor 50x/0.8 NA objective (Nikon) with white light emitted by a halogen lamp. The focal spot full-width at half-maximum equals 14  $\mu\text{m}$ . The collected light is dispersed by a diffraction grating (150 lines mm, blazed at 500 nm). Two linear polarizers in the excitation and collection path are used to select the s- or p- polarization. Angular-resolved reflectance is obtained by replacing the cavity with a commercial mirror, which allows to normalize the spectra reflected off the cavity at each angle with those obtained with the mirror at the corresponding angles. Angular-resolved steady-state fluorescence is measured by pumping the coupled cavity with a 473 nm continuous wave laser (Excelsior 473, Spectra Physics) coupled to the Fourier microscope in epi-illumination configuration and focused down to 1  $\mu\text{m}$ . The laser power is attenuated to 30 mW to avoid local damaging of the sample. The pump laser is filtered by a 500 nm long pass filter and its polarization is selected by the same broadband linear polarizer used for reflectance. The measurements for different detunings are collected using the same integration time to ensure comparability.

Lifetime measurements are performed by a homemade time-correlated single-photon counting module coupled to the Fourier microscope. 100 ps laser pulses centered around 513 nm (LDH-P-C-520M, PicoQuant) are focused on the sample surface by the same epi-illumination path used for the steady-state fluorescence. We use a repetition rate of 10 MHz and an intensity such that the average photon count rate at the detector is always 0.04% of the excitation rate. The focus diameter is roughly 1  $\mu\text{m}$ . The pump beam is filtered by a 525 nm long pass filter, while the appropriate 10 nm full-width at half-maximum band pass filter selects the LP or MP normal incidence wavelength, for each detuning. The emitted light follows the same optical path as reflectance and steady-state fluorescence but is directed to a single-photon avalanche photodiode (MPD). The trigger from the laser driver (PDL 800-D, PicoQuant) and the signal from the detector are sent to a time-to-digital converter (Time Tagger 20, Swabian Instruments). All histograms are built with 100 ps binwidth. The instrument response function (IRF) has been measured in several ways to check consistency of the result and ensure a reliable exponential fit for the short-time dynamics.

The relation between reflectance, fluorescence and decay measurements is guaranteed by the overlapping focus spots and the slow gradient slope of the PMMA layer thickness.

#### *Detuning-resolved measurements*

In order to access experimentally a large set of detunings in a single sample, we designed the PMMA layer to exhibit a slow and almost linear gradient towards the peripheral zones. This radial gradient is controlled by the spin-coating rotation speed. A radial sample movement of one millimeter corresponds to increasing the PMMA thickness by approximately 50 nm. On the other hand, the ErB/PVA layer featured a constant thickness throughout the sample. The position of the focal spot is controlled by micrometer screws that permit shifting the sample in the focal plane of the microscope objective.

*Theoretical approach.*- The Green's functions follows the Dyson equation  $\mathcal{G}^{-1}(z) = [\mathcal{G}^{(0)}(z)]^{-1} - \Sigma(z)$ , with the non-vanishing terms

$$\mathcal{G}_{11}^{(0)}(z) = \frac{1}{z - \omega_c^L(\theta)}, \quad \mathcal{G}_{22}^{(0)}(z) = \frac{1}{z - \omega_c^R(\theta)} \quad (4)$$

$$\mathcal{G}_{33}^{(0)}(z) = \frac{1}{z - \omega_X},$$

and the self-energy given by

$$\Sigma_{12}(z) = \Sigma_{21}(z) = -t, \quad (5)$$

$$\Sigma_{23}(z) = \Sigma_{32}(z) = \Omega.$$

The Green's function can be obtained analytically in this case, in particular, we obtain

$$\mathcal{G}_{11}(z) = \frac{1}{\mathcal{G}_{11}^{(0)}(z) - t^2 \mathcal{G}_{11}^{(0)}(z - \Omega^2 \mathcal{G}_{33}^{(0)}(z))}. \quad (6)$$

After analytic continuation  $z \rightarrow \omega + i0^+$ , the energies of the polaritons are obtained by the position of the poles of the Green's function

$$\text{Re}[\mathcal{G}_{11}^{-1}(E)] = 0, \quad (7)$$

which has the three solutions coined lower, middle, and upper polariton. The residue

$$Z = \left( \frac{\partial \text{Re}[\mathcal{G}_{11}^{-1}(\omega)]}{\partial \omega} \right)^{-1} \Bigg|_{\omega=E}. \quad (8)$$

The dispersion of the cavity photons is given  $\omega_c^{(R/L)}(\mathbf{k}) = \frac{c}{n_c^{(R/L)}} \sqrt{k_z^2 + k_{\parallel}^2}$ , where the incident light is along the  $z$  axis, perpendicular to the cavity mirrors, where the angle  $\theta$ , is given by  $k_{\parallel} = n_c^{(R/L)} \frac{\omega}{c} \sin \theta$ .

*Acknowledgments.*- We thank Joel Yuen-Zhou for the critical reading to our manuscript and valuable discussions. G. P. acknowledges financial support from Grants UNAM DGAPA PAPIIT No. IN104522 and CONA-CyT projects 1564464 and 1098652. H. L. G. acknowledges financial support from Grant UNAM DGAPA PAPIIT No. IA107023. A. C. G. acknowledges financial support from Grant UNAM DGAPA PAPIIT No. IN108620. C. L. O-R acknowledges financial support from Grant UNAM DGAPA PAPIIT IG100521.

H.E.S. acknowledges support from DGTIC-UNAM under Project LANCAD-UNAM-DGTIC-419 and from Grant UNAM DGAPA PAPIIT No. IA106023. A.C.-G, G. P. and H. E. S acknowledge financial support of PIIIF 2023 H.E.S, acknowledges Carlos Ernesto López Natarén for helping with the high-performance computing infrastructure. H. A. L.-G, A.C.-G, G. P acknowledge support from Grant UNAM DGAPA PAPIME No. PE101223.

Contributions

Y.A.G.-C, B. V., D. L. D, C. L. O.-R., H. L.-G, and G. P performed the experiments. R. A, H. E. S., and A. C.-G provided the theoretical analysis. H. A. L.-G., A. C. -G and G. P wrote the paper, with input from all authors. A. C.-G and G. P. designed the project.

Corresponding authors

Correspondence to Arturo Camacho Guardian and Giuseppe Pirruccio.

- 
- [1] Oleg Derzhko, Johannes Richter, and Mykola Maksymenko, “Strongly correlated flat-band systems: The route from heisenberg spins to hubbard electrons,” *International Journal of Modern Physics B* **29**, 1530007 (2015).
- [2] Leon Balents, Cory R Dean, Dmitri K Efetov, and Andrea F Young, “Superconductivity and strong correlations in moiré flat bands,” *Nature Physics* **16**, 725–733 (2020).
- [3] Päivi Törmä, Sebastiano Peotta, and Bogdan A Bernevig, “Superconductivity, superfluidity and quantum geometry in twisted multilayer systems,” *Nature Reviews Physics* **4**, 528–542 (2022).
- [4] Haidong Tian, Xueshi Gao, Yuxin Zhang, Shi Che, Tianyi Xu, Patrick Cheung, Kenji Watanabe, Takashi Taniguchi, Mohit Randeria, Fan Zhang, *et al.*, “Evidence for dirac flat band superconductivity enabled by quantum geometry,” *Nature* **614**, 440–444 (2023).
- [5] Kai Sun, Zhengcheng Gu, Hosho Katsura, and S Das Sarma, “Nearly flatbands with nontrivial topology,” *Physical review letters* **106**, 236803 (2011).
- [6] T. Jacqmin, I. Carusotto, I. Sagnes, M. Abbarchi, D. D. Solnyshkov, G. Malpuech, E. Galopin, A. Lemaître, J. Bloch, and A. Amo, “Direct observation of dirac cones and a flatband in a honeycomb lattice for polaritons,” *Phys. Rev. Lett.* **112**, 116402 (2014).
- [7] Sebabrata Mukherjee, Alexander Spracklen, Debadiya Choudhury, Nathan Goldman, Patrik Öhberg, Erika Andersson, and Robert R. Thomson, “Observation of a localized flat-band state in a photonic lieb lattice,” *Phys. Rev. Lett.* **114**, 245504 (2015).
- [8] Falko Diebel, Daniel Leykam, Sebastian Kroesen, Cornelia Denz, and Anton S Desyatnikov, “Conical diffraction and composite lieb bosons in photonic lattices,” *Physical Review Letters* **116**, 183902 (2016).
- [9] Sebabrata Mukherjee, Alexander Spracklen, Manuel Valiente, Erika Andersson, Patrik Öhberg, Nathan Goldman, and Robert R Thomson, “Experimental observation of anomalous topological edge modes in a slowly driven photonic lattice,” *Nature communications* **8**, 13918 (2017).
- [10] Tomoki Ozawa, Hannah M Price, Alberto Amo, Nathan Goldman, Mohammad Hafezi, Ling Lu, Mikael C Rechtsman, David Schuster, Jonathan Simon, Oded Zilberberg, *et al.*, “Topological photonics,” *Reviews of Modern Physics* **91**, 015006 (2019).
- [11] Lene Vestergaard Hau, Stephen E Harris, Zachary Dutton, and Cyrus H Behroozi, “Light speed reduction to 17 metres per second in an ultracold atomic gas,” *Nature* **397**, 594–598 (1999).
- [12] F Massou, “Electromagnetically induced transparency with tunable single-photon pulses,” *Nature* **438**, 837–841 (2005).
- [13] “Dark-state polaritons in electromagnetically induced transparency,” *Physical review letters* **84**, 5094 (2000).
- [14] M. Fleischhauer and M. D. Lukin, “Quantum memory for photons: Dark-state polaritons,” *Phys. Rev. A* **65**, 022314 (2002).
- [15] Matthew S. Bigelow, Nick N. Lepeshkin, and Robert W. Boyd, “Superluminal and slow light propagation in a room-temperature solid,” *Science* **301**, 200–202 (2003), <https://www.science.org/doi/pdf/10.1126/science.1084429>.
- [16] Shuyuan Xiao, Tao Wang, Tingting Liu, Xicheng Yan, Zhong Li, and Chen Xu, “Active modulation of electromagnetically induced transparency analogue in terahertz hybrid metal-graphene metamaterials,” *Carbon* **126**, 271–278 (2018).
- [17] S. E. Harris, J. E. Field, and A. Imamoglu, “Nonlinear optical processes using electromagnetically induced transparency,” *Phys. Rev. Lett.* **64**, 1107–1110 (1990).
- [18] M. D. Lukin and A. Imamoglu, “Nonlinear optics and quantum entanglement of ultraslow single photons,” *Phys. Rev. Lett.* **84**, 1419–1422 (2000).
- [19] Dmitri N Basov, Ana Asenjo-Garcia, P James Schuck, Xiaoyang Zhu, and Angel Rubio, “Polariton panorama,” *Nanophotonics* **10**, 549–577 (2020).
- [20] K.-J. Boller, A. Imamoglu, and S. E. Harris, “Observation of electromagnetically induced transparency,” *Phys. Rev. Lett.* **66**, 2593–2596 (1991).
- [21] Michael Fleischhauer, Atac Imamoglu, and Jonathan P Marangos, “Electromagnetically induced transparency: Optics in coherent media,” *Reviews of modern physics* **77**, 633 (2005).
- [22] Kati Stranius, Manuel Hertzog, and Karl Börjesson, “Selective manipulation of electronically excited states through strong light-matter interactions,” *Nature Communications* **9**, 2273 (2018).
- [23] Elad Eizner, Luis A Martínez-Martínez, Joel Yuen-Zhou, and Stéphane Kéna-Cohen, “Inverting singlet and triplet excited states using strong light-matter coupling,” *Science Advances* **5**, eaax4482 (2019).
- [24] Bo Xiang, Raphael F Ribeiro, Yingmin Li, Adam D Dunkelberger, Blake B Simpkins, Joel Yuen-Zhou, and Wei Xiong, “Manipulating optical nonlinearities of molecular polaritons by delocalization,” *Science advances* **5**, eaax5196 (2019).
- [25] Mónica Sánchez-Barquilla, Antonio I Fernández-Domínguez, Johannes Feist, and Francisco J García-Vidal, “A theoretical perspective on molecular polaritons,” *Physical Review Letters* **124**, 033901 (2020).

- tonics,” *ACS photonics* **9**, 1830–1841 (2022).
- [26] Jonathan Keeling and Stéphane Kéna-Cohen, “Bose–einstein condensation of exciton-polaritons in organic microcavities,” *Annual Review of Physical Chemistry* **71**, 435–459 (2020).
- [27] Claudia Climent, Fco García Vidal, Johannes Feist, *et al.*, “Cavity-modified chemistry: towards vacuum-field catalysis,” *Effects of electric fields on structure and reactivity: new horizons in chemistry* (2021).
- [28] Rocío Sáez-Blázquez, Johannes Feist, Elisabet Romero, Antonio I Fernández-Domínguez, and Francisco J García-Vidal, “Cavity-modified exciton dynamics in photosynthetic units,” *The Journal of Physical Chemistry Letters* **10**, 4252–4258 (2019).
- [29] Rui Su, Sanjib Ghosh, Jun Wang, Sheng Liu, Carole Diederichs, Timothy CH Liew, and Qihua Xiong, “Observation of exciton polariton condensation in a perovskite lattice at room temperature,” *Nature Physics* **16**, 301–306 (2020).
- [30] Natalia G Berloff, Matteo Silva, Kirill Kalinin, Alexis Askitopoulos, Julian D Töpfer, Pasquale Cilibrizzi, Wolfgang Langbein, and Pavlos G Lagoudakis, “Realizing the classical xy hamiltonian in polariton simulators,” *Nature materials* **16**, 1120–1126 (2017).
- [31] Alexey Kavokin, Timothy CH Liew, Christian Schneider, Pavlos G Lagoudakis, Sebastian Klemmt, and Sven Höfling, “Polariton condensates for classical and quantum computing,” *Nature Reviews Physics* **4**, 435–451 (2022).
- [32] Masamitsu Amano, Kazuhito Otsuka, Tohru Fujihara, Hisao Kondo, and Kazuki Bando, “Slow-light dispersion of a cavity polariton in an organic crystal microcavity,” *Applied Physics Letters* **120** (2022).
- [33] A. R. A. Chalcraft, S. Lam, B. D. Jones, D. Szymanski, R. Oulton, A. C. T. Thijssen, M. S. Skolnick, D. M. Whittaker, T. F. Krauss, and A. M. Fox, “Mode structure of coupled 13 photonic crystal cavities,” *Opt. Express* **19**, 5670–5675 (2011).
- [34] Milad Jahangiri, Fatemeh Moradiani, Gholam-Mohammad Parsanasab, and Mohsen Mirmohammadi, “High side-mode suppression ratio with a vernier effect single-mode laser using triple coupled microrings,” *Scientific Reports* **13**, 7092 (2023).
- [35] Haotian Wang, Sheng Liu, Lin Chen, Deyuan Shen, and Xiang Wu, “Dual-wavelength single-frequency laser emission in asymmetric coupled microdisks,” *Scientific Reports* **6**, 38053 (2016).
- [36] Marco Abbarchi, A Amo, VG Sala, DD Solnyshkov, H Flayac, L Ferrier, I Sagnes, E Galopin, A Lemaître, G Malpuech, *et al.*, “Macroscopic quantum self-trapping and josephson oscillations of exciton polaritons,” *Nature Physics* **9**, 275–279 (2013).
- [37] Konstantinos G Lagoudakis, B Pietka, M Wouters, Régis André, and Benoit Deveaud-Plédran, “Coherent oscillations in an exciton-polariton josephson junction,” *Physical review letters* **105**, 120403 (2010).
- [38] Matthew Du, Raphael F Ribeiro, and Joel Yuen-Zhou, “Remote control of chemistry in optical cavities,” *Chem* **5**, 1167–1181 (2019).
- [39] Yesenia A García Jomaso, Brenda Vargas, David Ley Domínguez, César L Ordoñez-Romero, Hugo A Lara-García, Arturo Camacho-Guardian, and Giuseppe Pirruccio, “Fate of the upper polariton: Breakdown of the quasiparticle picture in the continuum,” *Physical Review B* **107**, L081302 (2023).
- [40] Jesper Levinsen, Guangyao Li, and Meera M. Parish, “Microscopic description of exciton-polaritons in microcavities,” *Phys. Rev. Res.* **1**, 033120 (2019).
- [41] Shima Rajabali, Erika Cortese, Mattias Beck, Simone De Liberato, Jérôme Faist, and Giacomo Scalari, “Polaritonic nonlocality in light–matter interaction,” *Nature Photonics* **15**, 690–695 (2021).
- [42] Zefang Wang, Daniel A Rhodes, Kenji Watanabe, Takashi Taniguchi, James C Hone, Jie Shan, and Kin Fai Mak, “Evidence of high-temperature exciton condensation in two-dimensional atomic double layers,” *Nature* **574**, 76–80 (2019).
- [43] Bastian Miller, Alexander Steinhoff, Borja Pano, Julian Klein, Frank Jahnke, Alexander Holleitner, and Ursula Wurstbauer, “Long-lived direct and indirect interlayer excitons in van der waals heterostructures,” *Nano letters* **17**, 5229–5237 (2017).
- [44] Ying Jiang, Shula Chen, Weihao Zheng, Biyuan Zheng, and Anlian Pan, “Interlayer exciton formation, relaxation, and transport in tmd van der waals heterostructures,” *Light: Science & Applications* **10**, 72 (2021).
- [45] Long Zhang, Fengcheng Wu, Shaocong Hou, Zhe Zhang, Yu-Hsun Chou, Kenji Watanabe, Takashi Taniguchi, Stephen R Forrest, and Hui Deng, “Van der waals heterostructure polaritons with moiré-induced nonlinearity,” *Nature* **591**, 61–65 (2021).
- [46] Arturo Camacho-Guardian and Nigel R Cooper, “Moiré-induced optical nonlinearities: single-and multiphoton resonances,” *Physical Review Letters* **128**, 207401 (2022).
- [47] Alberto Ciarrocchi, Fedele Tagarelli, Ahmet Avsar, and Andras Kis, “Excitonic devices with van der waals heterostructures: valleytronics meets twistrionics,” *Nature Reviews Materials* **7**, 449–464 (2022).

## I. $\Lambda$ -SCHEME: THEORETICAL DETAILS

We consider the imaginary-time Green's function defined as  $\mathcal{G}_{\alpha,\beta}(\tau) = -\langle T_\tau[\hat{\psi}_\alpha(\tau)\hat{\psi}_\beta^\dagger(0)] \rangle$ , here the subindices  $\alpha, \beta$  correspond to the left/right cavity photon and exciton, respectively. The Dyson's equation  $\mathcal{G}^{-1}(z) = [\mathcal{G}^{(0)}(z)]^{-1} - \Sigma(z)$ , is given in terms of the ideal  $\mathcal{G}^{(0)}(z)$  Green's function which define a diagonal matrix

$$\mathcal{G}_{11}^{(0)}(z) = \frac{1}{z - \omega_c^L(\theta)}, \quad \mathcal{G}_{22}^{(0)}(z) = \frac{1}{z - \omega_c^R(\theta)}, \quad \mathcal{G}_{33}^{(0)}(z) = \frac{1}{z - \omega_X}. \quad (9)$$

The self-energy gives the coupling between the left and right cavity photons  $\Sigma_{12}(z) = \Sigma_{21}(z) = -t$ , with  $t$  the tunneling coefficient. The light-matter coupling between the excitons and right cavity photons is given by  $\Sigma_{23}(z) = \Sigma_{32}(z) = \Omega$ .

In this case, as mentioned in the main text, the Green's function acquires an analytical form, in particular, the Green's function of the left cavity photons is given by

$$\mathcal{G}_{11}(z) = \frac{1}{z - \omega_c^L(\theta) - \frac{t^2}{z - \omega_c^R(\theta) - \frac{\Omega^2}{z - \omega_X}}}. \quad (10)$$

If  $\omega_c^R(\theta)$  is detuned from the exciton energy and following the branch of the middle polariton we obtain

$$\mathcal{G}_{11}(\omega_X + \omega) \approx \frac{1}{\omega_X + \omega - \omega_c^L(\theta) - \frac{t^2}{\Omega^2}(\omega)}. \quad (11)$$

The pole is found at

$$\omega(\theta) = \frac{[\omega_c^L(\theta) - \omega_X]}{1 + \left(\frac{t}{\Omega}\right)^2}, \quad (12)$$

that is, the energy of the middle polariton is given by  $\omega_{\text{MP}}(\theta) = \omega_X + \frac{[\omega_c^L(\theta) - \omega_X]}{1 + \left(\frac{t}{\Omega}\right)^2}$  as given in the main text. This holds as long as the energy shift remains within the energy window  $|\omega(\theta)| \ll \frac{t^2}{|\omega_X - \omega_c^R|}$ .

The broadening of the photon and exciton lines can be included via additional terms which account for the losses. Then, the experimental model departs from the idealized scenario discussed before. The broadening of the right cavity photons reduces the energy window  $\frac{t^2}{\sqrt{(\gamma_c^R)^2 + |\omega_X - \omega_c^R|^2}}$ , while the broadening of the exciton lines leads to imperfect slow-light where the right cavity photons remains coupled to the middle polariton even at resonance  $\omega_c^R(\theta = 0) = \omega_X$ . This coupling is small as long as  $\sqrt{(\gamma_c^R)^2 + |\omega_X - \omega_c^R|^2} \ll t^2/\gamma_X$ . We estimate the ratio

$$\frac{t^2}{(\gamma_X \sqrt{(\gamma_c^R)^2 + |\omega_X - \omega_c^R|^2})} \approx 10 - 50$$

that is, we expect to see clear signatures of slow-light with right cavity photons effectively decoupled from the middle polaritons under resonant conditions.

In Fig. 4 we show the spectral function at normal incidence of the left (a) and right (b) cavity photons as a function of the detuning  $\delta = \delta_{LX}$ . The vanishing value of the spectral function  $A_{22}(\mathbf{0}, \omega)$  around zero detuning signals the full decoupling of the right cavity photon from the middle polariton.

The vanishing of the right cavity photon component on the middle polariton is equivalent to the transparency window observed in electromagnetically induced transparency. This implies that the possibility to observe the middle polariton depends on the arrangement of the stacked cavities. In particular, we observe the middle polariton in reflectance as light is injected from the left cavity. If light were injected from the right cavity, then the reflectance spectrum would not signal the presence of this branch. For the same reason, transmittance would not reveal the MP branch. In this sense, the middle polariton is dark under certain circumstances.

## II. EMERGENCE OF A FLATBAND

We now show additional experimental data that further illustrate the emergence of an intercavity polariton with a flatband dispersion. As explained in the main text, the polariton bands depend on the tunneling ratio, the Rabi

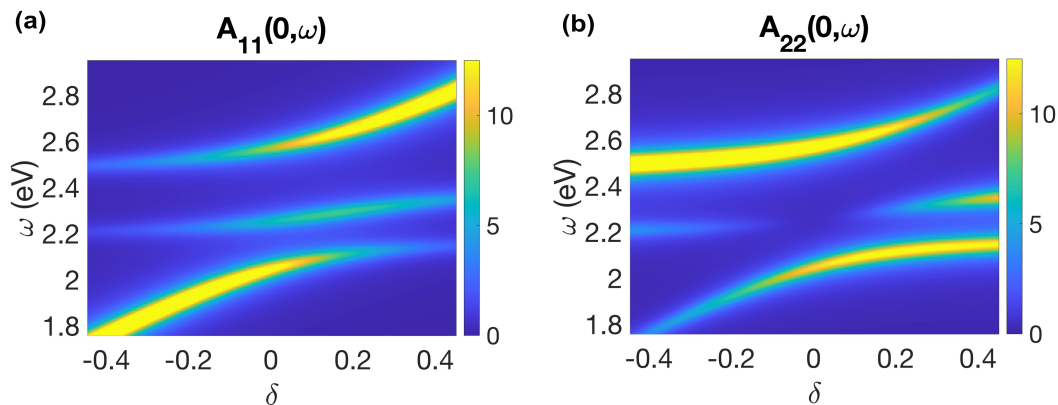


FIG. 4. Spectral function of the (a) Left and (b) Right cavity photons as a function of the left cavity detuning,  $\delta = \delta_{LX}$ . Around zero detuning we observe that the middle polariton decouples from the right cavity photon.

splitting, and the different energy levels. We introduce the cavity detuning from the exciton energy at normal incidence  $\delta_{LX} = \omega_c^{(L)}(\theta = 0) - \omega_X$  and  $\delta_{RX} = \omega_c^{(R)}(\theta = 0) - \omega_X$ .

Figures 5 (a)-(b) show the reflectance spectrum for varying detuning  $\delta_{LX}$  with the remaining parameters as detailed in Table [1]. From left to right we observe the emergence of a purely middle intercavity polariton formed by a left cavity photon and an exciton localized in the right cavity. This is demonstrated by the quasiparticle residues shown in the bottom of Figs. 5 (a)-(b).

Fig. 4	$\delta_{LX}$ [eV]	$\delta_{RX}$ [eV]	$t$ [eV]	$2\Omega$ [eV]	$\omega_X$ [eV]
a	-0.37	0.12	0.21	0.26	2.23
b	-0.18	0.09	0.21	0.26	2.23
c	-0.08	0.13	0.21	0.26	2.23
d	-0.03	0.13	0.21	0.26	2.23
e	0.00	0.17	0.23	0.245	2.25
f	0.07	0.15	0.21	0.26	2.23

Table 1. Theoretical parameters of the polariton branches in Fig. 5.

The evolution of the MP Hopfield coefficients illustrate that, as the left cavity detuning is driven to  $\delta_{LX} = 0$ , the right cavity photon decouples from the MP causing the suppression of its dispersion. For  $\delta_{LX} = 0$ , although the polariton energy matches the bare exciton, the MP does not lose its photonic character because it retains significant residue of the right cavity photon.

In Fig. 6 we show the evolution of the fluorescence as a function of the detuning. Pumping the system at  $\omega_p = 2.62$  eV ensures that for  $\delta = \delta_{LX} = 0$  we drive coherently the UP which consists primarily of right cavity photons. The absence of the left photonic component in the driven UP strongly suppresses the emission of the MP for  $\delta = \delta_{LX} = 0$

We should note that the right cavity photons are the dominant component of the UP in all of our cavity detunings. However, as we drive at  $\omega_p = 2.62$  eV, for large negative detuning, this driving is off-resonant, that is, it lies far above the energy of the upper polariton, and thus, photons are injected in left and right cavities. Therefore, for negative detunings, we observe emission from both the middle and lower polariton branches.

### III. POLARITON DYNAMICS

In the main text we focus on the short-time dynamics of the polaritons. Here, we provide the experimental data in an extended time window. Figure 7 shows the LP (a) and MP (b) fluorescence decay for  $\delta_{LX}/\text{eV} = -0.37$  (blue), on resonance  $\delta_{LX}/\text{eV} = 0$  (purple) and  $\delta_{LX}/\text{eV} = 0.20$  (green). The shaded pink area corresponds to the time window discussed in the main text where we focused on the initial decay. As a consequence of the coupling to the triplet state by intersystem crossing for large negative detunings, or to the bare exciton states for positive detunings, the decay of the LP for  $t > 10$  ns after the laser pulse arrival becomes more complex. In the former case, where the energy of the LP

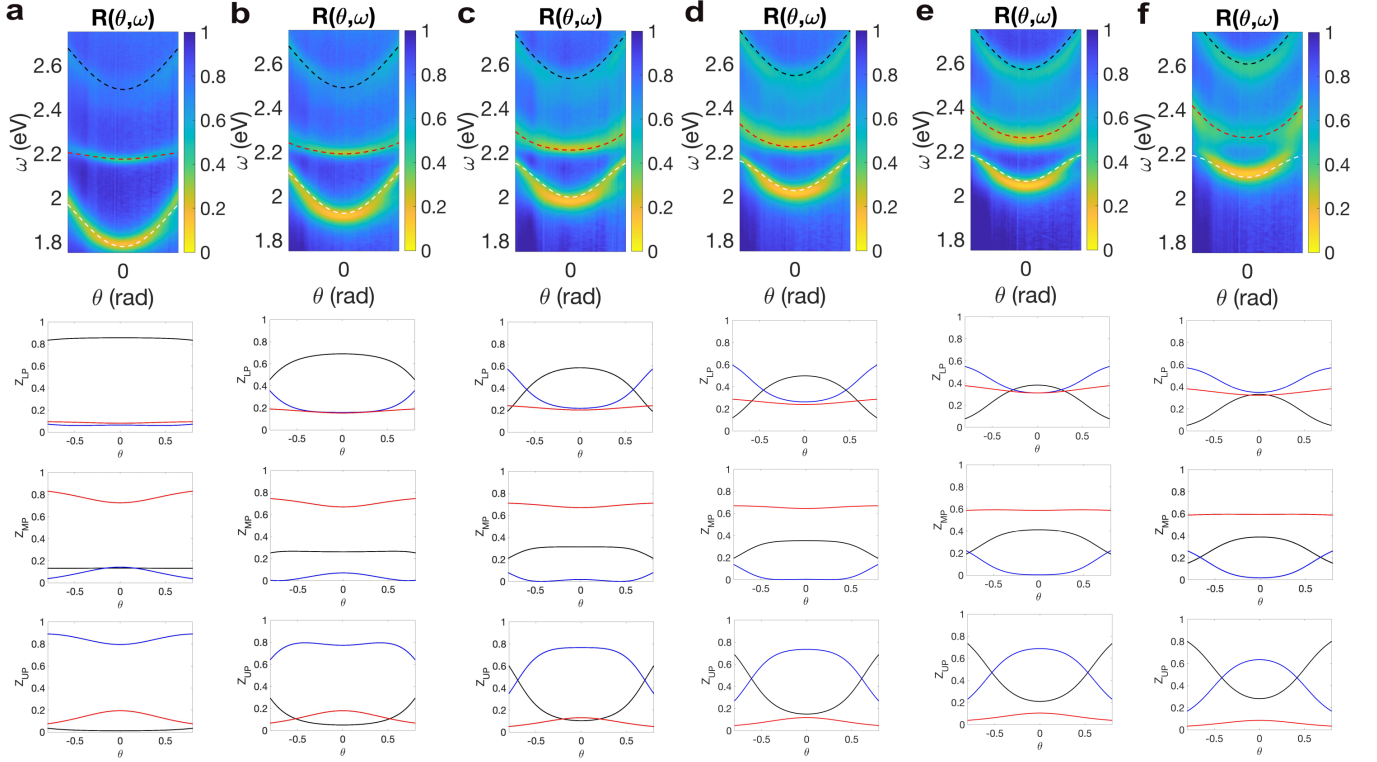


FIG. 5.  $s$ -polarized reflectance as a function of the incident angle and the energy for several cavity detunings. The dashed curves represent the energies of the three polariton branches, obtained with the parameters given in Table [1]. In the bottom row, we show the quasiparticle residues, i.e., the Hopfield coefficients, of the three quasiparticle branches following the color code of the main text.

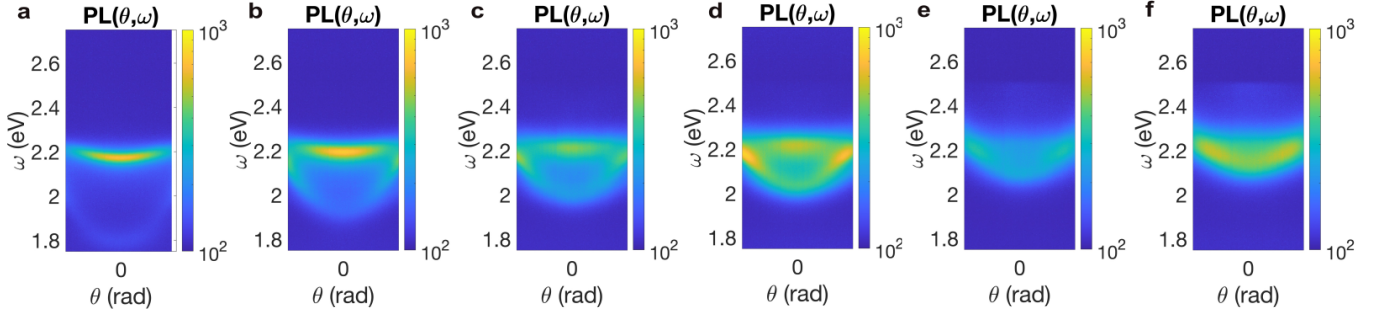


FIG. 6.  $s$ -polarized fluorescence for the same parameters as in Fig. 5 and Table 1. From left to right we observe a strong suppression of the MP fluorescence as the left cavity detuning approaches zero.

approaches the triplet state, we see the presence of a long-living state which does not decay entirely in the considered time window. A similar effect, although less pronounced, is seen as the LP shifts toward the bare exciton energy. An intermediate situation is observed for detunings around  $\delta_{LX}/\text{eV} = -0.2$ . The ability to control the dynamics of the LP was extensively discussed for a single cavity [22].

On the other hand, the MP energy lies very far away from the triplet state, thus the triplet state does not participate in the MP dynamics and its decay is given by the slow-light physics discussed in the main text. For  $t > 10\text{ns}$  after the laser pulse arrival, the MP time evolution resembles the dynamics of the ErB/PVA thin film in the absence of the cavity. This can be appreciated by comparing the black curve in Fig. 7(b) with the MP decays.

In Fig. 7(b) we show with red curve the IRF obtained by measuring a 0.5 M solution of ErB in water which is known to decay mono-exponentially with a lifetime well below the time resolution of our instrument. This choice ensures that the detector wavelength-dependent response does not play a role in our measurements. The same experimental conditions as for the cavity measurements are used. The full-width at half-maximum of this decay is approximately

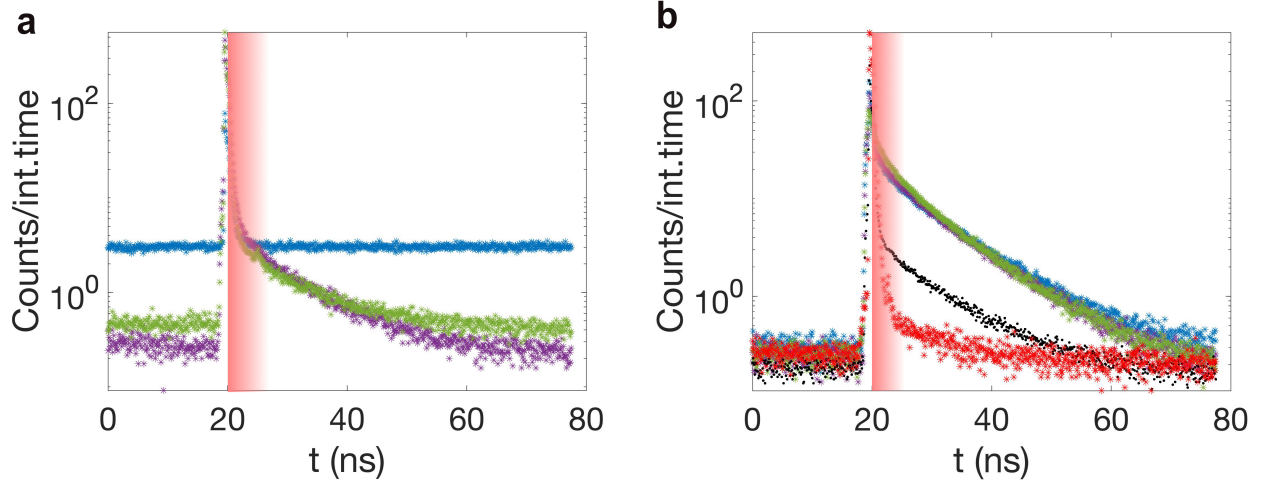


FIG. 7. Fluorescence decays of the LP (a) and MP (b) for different cavity detunings:  $\delta_{LX}/\text{eV} = -0.37$  (blue), on resonance  $\delta_{LX}/\text{eV} = 0.00$  (purple) and  $\delta_{LX}/\text{eV} = 0.20$  (green). In (b), the black curve represents the decay of the ErB/PVA thin film in the absence of the cavity, while the red curve corresponds to the IRF. The shaded pink area corresponds to the time window discussed in the main text.

350 ps. Having characterized the IRF curve, the short-time fit of the LP and MP decays can be safely conducted by excluding the first 600 ps after the intensity maximum. This time value is labelled as  $t = 0$  ns in Fig.3(a) of our manuscript.

It is important to highlight that within the shaded pink area, i.e., within the first 10 ns from the arrival of the laser pulse, the dynamics of the ErB molecule in absence of the cavity can be excellently modeled by a single exponential. We find that  $A = 0.9$ ,  $\Gamma = 4.9 \text{ ns}^{-1}$  and  $\eta = 0.24 \text{ ns}^{-1}$ . Thus the rich interplay observed for the MP and its overall slow dynamics cannot be accounted for with the ErB photophysics.